PORTABLE X-RAY FLUORESCENCE IDENTIFICATION OF THE CRETACEOUS-PALEOGENE BOUNDARY: APPLICATION TO THE AGOST AND CARAVACA SECTIONS, SE SPAIN

Jordi Ibáñez-Insa,[1] Jordi Pérez-Cano,[2] Víctor Fondevilla,[2] Oriol Oms,[2] Marta Rejas,[1], José. L. Fernández-Turiel[1], and Pere Anadón[1]

[1]Institute of Earth Sciences Jaume Almera, ICTJA-CSIC, Lluís Solé i Sabarís s/n, E-08028 Barcelona, Catalonia, Spain

[2]Unitat d'Estratigrafia, Departament de Geologia, Universitat Autònoma de Barcelona, Edifici C, E-08193 Bellaterra (Barcelona), Catalonia, Spain

We show that portable x-ray fluorescence (pXRF) is a powerful tool for the unambiguous identification and geochemical characterization of prospective Cretaceous-Paleogene (K-Pg) boundary sites. We have performed in-situ analyses in two well-known K-Pg boundary sequences, located at Agost and Caravaca, SE Spain. A sizable enrichment around the K-Pg horizon of several elements such as K, Ti, Fe, Ni, Cr, Cu, Zn, As or Pb, together with a strong reduction in the Ca content, is found with the pXRF instrument. These observations represent a primary geochemical signature of the K-Pg boundary in distal marine sections such as those of Agost and Caravaca. We show that the intensities of the XRF peaks correlate well with elemental composition data obtained by inductively coupled plasma-mass spectrometry (ICP-MS) on collected samples. Hence, the pXRF field measurements are shown to provide fast and useful quantitative information about K-Pg boundary sequences.

Keywords: X-ray fluorescence spectrometry, Cretaceous-Tertiary boundary, geochemistry, Chicxulub impact, Deccan traps

Corresponding author:
Jordi Pérez-Cano
Present address
Departament de Geologia (Estratigrafia), Facultat de Ciències, Universitat Autònoma de Barcelona,
Carrer de l'eix Central, 08193, Cerdanyola del Vallès, Barcelona, Catalonia, Spain
Email address: perezcanojordi@gmail.com

1. Introduction

The Cretaceous-Paleogene (K-Pg) boundary (or Cretaceous-Tertiary (K-T) boundary) occurred around 66 million years ago and marks one of the 'Big Five' mass extinctions in Earth's history (Raup and Sepkosky, 1982). Although different hypothesis such as massive flood basalt volcanism in the Deccan Plateau, India, have been proposed to explain the K-Pg event (Keller, 2014; Schoene et al., 2014), it is widely accepted that it was triggered by the collision of a large meteorite (~10 km in diameter) on the Yucatan Peninsula, Mexico, giving rise to the Chicxulub crater (Alvarez et al., 1980; Schulte et al., 2010, Renne et al., 2013).

The K-Pg boundary records characteristic micropaleontological, geochemical and mineralogical fingerprints that have enabled numerous identifications in marine sections worldwide (Schulte et al. (2010) and references therein). It is well known that the K-Pg boundary can be identified with one or more of the following observations: (i) turnover of numerous microfossils like those of benthic and planktonic foraminifera (Culver, 2003; Alegret, 2007); (ii) a change in lithology, with an abrupt reduction of biogenic calcareous content and the appearance of a 2 to 3-mm reddish, goethite-rich layer known as impact layer or ejecta layer, which is attributed to large amounts of impact ejecta that were dispersed globally and deposited in a very short period of time (Alvarez et al., 1980), and also to the acidification of oceanic water (Premović, 2011); (iii) the presence of the so-called boundary clay, i.e., a thin layer of clay-rich sediments just above the impact layer that were probably deposited during 40-50 kyr after the impact event (Alvarez et al., 1980; Premović, 2011; Schoene et al., 2014); (iv) enrichment in iridium and other platinum group elements (PGE) of presumably meteoritic origin in the impact layer (Alvarez et al., 1980); (v) observation of microtektite glass shperules, microkrystites and/or shocked minerals that are attributed to products generated during and after the impact (Montanari et al., 1983; Schulte et al., 2009; Belza et al., 2015); (vi) a strong negative anomaly in the $\delta^{13}C$ isotopic signature (Schoene et al., 2014), which is indicative of a decrease in primary productivity and release of plant-based carbon.

Most of the works published in the literature dealing with the identification and geochemical characterization of the K-Pg boundary at numerous sites around

the world dealt with the use of different laboratory techniques such as inductively-coupled mass spectrometry (ICP-MS), electron probe microanalysis (EPMA), x-ray fluorescence (XRF), x-ray diffraction (XRD), or stable isotope ratios analysis (see Schulte et al. (2010) and references therein). In order to identify new K-Pg boundary sites and also to further characterize those already known, the availability of portable analytical tools for in-situ measurements could be highly advantageous. In spite of the clear interest of field methods for this type of studies, only a few previous works have relied on in-situ analyses to recognize the K-Pg boundary. In particular, a magnetic susceptibility (MS) field method was successfully employed and later confirmed by inductively-coupled plasma mass spectrometry (ICP-MS) and particle-induced X-ray emission (PIXE) measurements to identify the K-Pg horizon in Oman (Ellwood et al., 2003).

In the past decade, portable XRF (pXRF) devices were widely adopted to obtain fast and non-destructive in-situ elemental information in many different research and industrial areas (see for instance Potts and West, 2008) such as: environmental research and soil pollution assessments; workplace monitoring; archaeology and cultural heritage; metal and alloy sorting; mineral prospecting and ore-grade evaluations; etc. With regard to geochemistry studies, pXRF has already been employed in different settings and scenarios (Gazley et al., 2011; Marsala et al., 2012; Hall et al., 2014; Bourke and Ross, 2015). Recently, the pXRF technique has been shown to be particularly well suited as a screening tool for lithogeochemical explorations (Piercey and Devine, 2014).

In the present work we explore the usefulness of pXRF for the in-situ identification and characterization of K-Pg boundary sites. For this purpose, we have performed XRF field measurements in two well-known marine K-Pg boundary locations in the SE Iberian Peninsula: the Agost and the Caravaca sections. Several previous works have reported comprehensive geochemical information on these two sections (Smit, 1990, 2004; Martínez-Ruiz et al., 1992, 1997), showing that they contain a complete sequence of events across the K-Pg horizon. Thus, both sections are useful case-study locations to assess the suitability of the pXRF technique for this type of investigation. Here we show that pXRF allows one to obtain highly valuable geochemical data on a number of major and trace elements related to the specific lithology of the K-Pg horizon, thus suggesting

that this technique may become a powerful tool for the unambiguous in-situ identification and characterization of possible new K-Pg boundary sites around the world. The pXRF technique could be particularly useful in sections where paleontological or geochemical information is fragmentary or where there is no evident lithologcal contrast marking the boundary.

2. Geological setting

The sections of Agost (Alacant) and Caravaca (Murcia) are located in the external zones of the Betic Cordillera (Southeast of the Iberian Peninsula, see Fig. 1), within the Quípar-Jorquera Formation. While the Agost section is situated next to the Agost-Castalla road and can be easily found, the Caravaca section is placed on top of a small valley (Barranco del Gredero) and is usually dumped in landfill, making its localization less straightforward.

The K-Pg boundary in these two sections has been widely studied both from paleontological (Culver, 2003; Alegret et al., 2003; Alegret, 2007), geochemical and petrographic points of view (Martínez-Ruiz et al., 1992, 1997; Smit, 2004). Stratigraphic sections at Agost and Caravaca are shown in Figs. 2 and 3, respectively. From the beginning of the Late Cretaceous epoch up to the Eocene (100-48 ma), bathyal hemipelagic environments developed in both areas (Vera et al., 1982). Hence, the Maastrichtian rocks (Upper Cretaceous, 72.1-66 ma) consist of grey hemipelagic marls which are very rich in foraminifera, ostracods and other microfossils (Molina et al., 2004). The top of the Maastrichtian unit is highly burrowed, i.e., plenty of trace fossils (ichnofossils). The 2-3 mm-thick impact layer containing the iridium and PGE anomaly as well as sizable amounts of microspherules is located on top of this unit. Materials from this layer and also from the boundary clay refill the burrows around the end of the Maastrichtian unit (Rodríguez-Tovar et al., 2005). As is typical of K-Pg sequences around the planet (Schulte et al., 2010), $CaCO_3$ is dramatically reduced at the K-Pg boundary. The boundary clay appears in both Agost and Caravaca sections as a layer of dark grey clay (see Figs. 2 and 3). On top of this layer, hemipelagic marls that register the Danian recovery (Paleocene, 66-62 ma) were deposited. These marls show both an

increase of the fossil content and increased $CaCO_3$ contents, most likely as a consequence of a global biotic recovery.

3. Methods

3.1. XRF measurements

In-situ energy-dispersive XRF (EDXRF) measurements were carried out by using a portable, battery-operated Bruker Tracer IV-Geo analyzer, which is equipped with a large area (30 mm^2) silicon drift detector and a 40 kV Rh x-ray tube. The measurements were performed at ambient conditions by applying large voltages (40 kV) to the tube in order to optimize the detection of heavy elements.

Although this XRF analyzer is specifically designed to work handheld, the in situ measurements were performed by setting the instrument in the field as bench-top instrument, for which purpose an appropriate mount was used. This allowed us to avoid the inaccuracies associated with the handheld mode of operation. Thus, small flakes of material were taken from both the Agost and Caravaca sections and directly positioned on top of the analyzer's window, which was protected with a 4.0-μm Prolene® film. No additional processing of the samples was carried out. The integration time for all the measurements was 90 s, which allowed us to record in situ all the data in less than 4 hours for each section (around 50 samples were measured per section).

In the field, real-time quantitative data obtained with one of the internal calibrations of the instrument, provided by the manufacturer, were displayed in a personal digital assistant (PDA) connected to the XRF analyzer. Although the in-built calibrations cannot be expected to provide reliable quantitative results, the data thus obtained were useful as a first, rough approximation to the metal enrichment of the sediments around the K-Pg boundary. In order to obtain more robust quantitative information, the intensity (i.e., the integrated area) of the XRF peaks was subsequently extracted by fitting the spectra with split pseudo-Voigt (SPV) functions for each of the detected XRF features. The intensities thus obtained were employed to monitor the elemental composition of the two sections, and additional ICP-MS measurements were carried out on 8 selected samples (see

below) to convert the raw XRF intensities into quantitative results. To avoid unnecessary processing of the data, no intensity corrections using the Compton or Rayleigh peaks were applied. In any case, the observed intensity variations of these features were usually lower than ~10% for samples with similar lithology.

3.2. Collection of microspherules and SEM-EDS measurements

In order to confirm the correct identification of the two K-Pg boundaries studied in this work, microspherules from the boundary clay and the impact layer of both sites were collected and investigated. The rock samples were mechanically disaggregated in distilled water and the microspherules were directly recovered from the > 53 μm fraction after sieving the disaggregated material by hand-picking, using a binocular microscope and wooden tool to avoid contamination. SEM-EDS analyses on gold-coated spherules were performed with a Zeiss EVO MAIO electron microscope. Figure 2 shows a typical SEM image of a microspherule from the Agost section. The average diameter of the spherules from both sections as measured from the SEM images ranged from 200 to 700 μm, in agreement with the observations of Smit (1990) and Martínez-Ruiz et al. (1997). Figure 2 also shows a selected EDS spectrum from the microspherules, which is dominated by strong signal from Fe, O and Si that can be attributed to a large content of iron oxides and silicates. Besides other elements like Al, S or Ti, weak signal from Ni is also observed. Similar observations, which can be attributed to the presence of Ni-rich spinels at the impact layer, have been reported in many previous works dealing with distal K-Pg boundary sequences worldwide (Keller et al., 1995; Martínez-Ruiz et al., 1997; Schoene et al., 2014).

3.3 Geochemical analyses by ICP-MS

High-resolution ICP-MS (HR-ICP-MS) whole-rock analyses were performed at LabGEOTOP laboratory, Institute of Earth Sciences Jaume Almera, CSIC, by using a Thermo Scientific Element XR system. The ICP-MS analysis was carried out on eight samples from the Caravaca section (4 samples were selected from the impact layer and/or the boundary clay, and 4 samples correspond to the Danian or

Maastrichtian marls). The samples were first dried during 24 h at 40 °C. Once crushed and grinded, 100 mg of sample were acid digested in closed PTFE vessels with a combination of HNO_3, HF, and $HClO_4$ (2.5 ml:5 ml:2.5 ml). After 12 hours, the samples were evaporated to near dryness and, afterwards, they were evaporated twice more by adding 1 ml of HNO_3 for two times. Finally, the final residue was made up to 100 ml with 1% HNO_3 (v/v) and MilliQ water (18.2 $M\Omega cm^{-1}$). The solution was stored at 4 °C until further analysis.

In this study, 49 isotopes were analysed: ^{23}Na, ^{27}Al, ^{31}P, ^{39}K, ^{43}Ca, ^{49}Ti, ^{54}Fe, ^{55}Mn, which were expressed as % oxides, and ^{7}Li, ^{9}Be, ^{45}Sc, ^{51}V, ^{52}Cr, ^{59}Co, ^{60}Ni, ^{63}Cu, ^{66}Zn, ^{69}Ga, ^{74}Ge, ^{75}As, ^{85}Rb, ^{88}Sr, ^{89}Y, ^{90}Zr, ^{93}Nb, ^{98}Mo, ^{120}Sn, ^{121}Sb, ^{133}Cs, ^{137}Ba, ^{139}La, ^{140}Ce, ^{141}Pr, ^{146}Nd, ^{147}Sm, ^{151}Eu, ^{157}Gd, ^{159}Tb, ^{162}Dy, ^{165}Ho, ^{166}Er, ^{169}Tm, ^{174}Yb, ^{175}Lu, ^{178}Hf, ^{208}Pb, ^{232}Th, and ^{238}U, which were expressed as parts per million (ppm or µg/g). In order to improve the sensitivity of the ICP-MS measurements, a tuning solution containing 1 $\mu g \cdot L^{-1}$ of Li, B, Na, K, Sc, Fe, Co, Cu, Ga, Y, Rh, In, Ba, Tl, and U was used, together with 20 $mg \cdot L^{-1}$ of a solution of ^{115}In as internal standard. The detection limit (LD) of the different elements was calculated as three times the standard deviation of the average of 10 blanks. The accuracy and precision of the ICP-MS analyses were determined with reference materials from the Geological Survey of Japan (andesite JA and basalt JB-3).

4. Results and discussion

Evidence for the expected enrichment of some elements such as Pb, Ni or Zn around the impact layer was readily obtained in-situ both at the Agost and Caravaca sections, as information about these elements was displayed in the portable XRF analyzer employed in this work. In the case of the sequence of Caravaca, the in-situ pXRF measurements were particularly helpful to unambiguously confirm the location of the K-Pg boundary, which was initially covered by recent rubble and was rather weathered, making its identification much more complicated. We would like to note that the boundary clay at Caravaca as shown in Fig. 3 was only visible after careful cleaning of the site.

Figures 4A and 4B show typical XRF spectra of samples from the impact layer and from the Maastrichtian unit from Agost and Caravaca. The XRF spectra of Danian

materials were very similar to those of the Maastrichtian samples and have not been included in the figure for clarity. As can be seen in both figures, the intensity of the XRF peaks corresponding to a number of major, minor and trace elements (K, Ti, Cr, Fe, Ni, Cu, Zn, As, Pb, Rb, Sr, Zr) exhibits a sizable increase at the impact layer. To a lower extent (not shown in the figure), similar results are found in the samples from the boundary clay. As can be observed in the spectra, elements like As, Pb or Cr are barely detected in the samples far above or below the boundary layer, whereas the intensity of the XRF peaks of these elements undergoes a dramatic increase at the impact layer. In contrast, both the Kα and Kβ peaks of Ca are largely reduced around the impact layer, which is a consequence of the abrupt reduction of $CaCO_3$ content associated with the boundary layer.

As is usual in this type of works, for the identification and analysis of the XRF spectra, different interferences between XRF features must be taken into account. In the present case, the most relevant interferences are the following peak overlaps: Ti Kα + V Kβ; Fe Kβ + Co Kα; As Kα + Pb Lα; Zr Kα + Sr Kβ. In contrast, Compton tail (CT) overlaps such as CT Fe Kα + Mn Kα or CT Ca Kα + K Kα are not found to yield large interferences, most likely because the K Kα and Mn Kα peaks are much stronger than their respective interfering CTs. As a consequence of these interferences, the present EDXRF measurements do not allow us to obtain reliable information about V and Co, both of which are expected to exhibit important anomalies at the K-Pg horizon (Martínez-Ruiz, 1992). In contrast, Pb, As and Zr can still be independently analysed by using the As Kβ, Pb Lβ and Zr Kβ secondary peaks.

Figure 5 shows an example of the fits to the XRF spectra that we have performed in order to extract the intensity of the XRF features and monitor the evolution of the detected elements along the two K-Pg boundary marine sections considered in this work. Excellent agreement between the calculated spectra and the experimental data, even for the Compton and Rayleigh peaks above 19 keV, is obtained with the SPV lineshapes. In order to translate XRF intensities into semi-quantitative data and obtain the corresponding calibration curves, ICP-MS measurements were carried out on 8 samples (4 samples were taken around the impact layer, and 4 samples were taken far away from it). The inset of Fig. 5 shows an example of calibration curve for the case of the Ni Kα peak. As can be seen in the

figure, a highly linear dependence between XRF intensities and Ni content (in ppm) as obtained by ICP-MS is found (R^2=0.992). Similar linear trends with R values close to 1 were observed for most of the detected XRF peaks; only in the case of Zr and Nb (not shown) lower R^2 values (~0.6) were obtained, which is a consequence of the very weak XRF signal of the non-interfering peaks used to analyze these two elements (see below).

Figures 6 (Agost) and 7 (Caravaca) show the intensity of several XRF peaks extracted with the fits (Ca Kα, Ti Kα, Cr Kα, Fe Kα, Ni Kα, Cu Kα, Zn Kα, As Kα + Pb Lα, As Kβ, Pb Lβ, and Zr Kβ) as a function of depth. In both figures, the intensity of all XRF features (lower abscissa axes) has been normalized to the maximum intensity value of each peak; a depth equal to zero corresponds to the K-Pg boundary. In all the plots of Figs. 6 and 7, semi-quantitative data as obtained from the different calibration curves constructed from the ICP-MS data can be read in the upper abscissa axes of each plot.

As these two figures illustrate, the XRF data provide clear evidence of whole-rock geochemical enrichments in several elements such as K (not shown for scaling reasons), Ti, Fe, Ni, Cr, Cu, Zn, As and Pb around the K-Pg boundary, accompanied by a reduction in Ca. These observations represent an unambiguous geochemical fingerprint of the K-Pg horizon. As can be seen in the plots around -20 cm and +20 cm (right panels), the enrichment is clearly more pronounced at the impact layer, while in the boundary-clay layer the intensity of the XRF peaks of the above elements is still larger than that measured in the Danian and Maastrichtian marls. We would like to note the particularly strong anomaly of the As Kα + Pb Lα peak at ~10.5 keV, which provides one of the clearest evidences of the K-Pg horizon in both sections.

In quantitative terms, as plotted on the upper horizontal axes in both Figs. 6 and 7, Fe content increases by a factor of ~10 (similar results are found for K, not shown), while Ca is found to decrease by a factor of ~8. Other elements like Ti, Cr, Cu, Zn or Pb, increase by a factor of around 10-25. In the case of Ni and As, dramatic increases of the order of 40 and 120, respectively, are found. While Ni is usually associated with Ni-rich spinels and connected to material from the impacting meteorite, the actual origin of the As anomaly has not been so far clarified. Recently, it has been hypothesized that such anomaly might be explained

by As adsorption from seawater by the Fe oxides that derived from the carbonaceous chondrite meteorite (Premović, 2015).

The enrichments determined with the in-situ pXRF measurements around the impact layers of Agost and Caravaca are in good agreement with the laboratory analyses on samples from these two sections (Martínez-Ruiz et al., 1992; Smit, 2004). Thus, it can be concluded that the pXRF technique not only provides a clear and consistent geochemical signature of the K-Pg horizon, but also allows one to obtain quantitative information for the geochemical characterization of K-Pg sequences.

Our XRF spectra also allowed us to monitor the evolution of other elements like Mn, Rb, Sr, Y, Zr and Nb (Figs. 6 and 7 only include the case of Zr). Light elements like Al, Si or P were not considered in this work because the excitation conditions of the field measurements were chosen to maximize the XRF signal from heavier (trace) elements. In the case of Mn, we did not observe any relevant change with depth in the intensity of the Kα peak, which suggests that this element does not exhibit any sizable variation around the impact layer. In contrast, we found some increase of Rb content at the K-Pg horizon in both sections, in agreement with Martínez-Ruiz et al., (1992). Also, we found a strong Sr anomaly in some of the samples of the impact layer in Agost (other samples from the same level even showed a small Sr depletion). Although this observation is in agreement with previous results (Martínez-Ruiz et al., 1992), we did not find any evidence for Sr enrichment at the sequence of Caravaca. Given that Sr may substitute Ca in $CaCO_3$, the analysis of the behaviour of this element is not straightforward and, as discussed in Martínez-Ruiz et al. (1992), the anomaly of Sr around the K-Pg boundary might be specifically related to detritic materials in the sedimentary basin of Agost. On the other hand, XRF peaks of Y, Zr and Nb were barely visible. Among these elements, Zr and Nb were found to exhibit some enrichment at the impact layer of both sequences (see Figs. 6 and 7 for the case of Zr; this element was monitored using the weak Kβ feature, since the Kα peak interferes with the Kβ peak of Sr). The ICP-MS data also show a tenfold increase in the concentration of Zr and Nb at the impact layer. Although no data for these two elements is reported in Martínez-Ruiz et al. (1992) or Smit (2004), a Zr anomaly was found at the K-Pg boundary in Oman (Ellwood et al., 2003), which suggests that a Zr enrichment may

also occur at Agost and Caravaca. This result further demonstrates the usefulness of the in-situ XRF measurements to identify and characterize K-Pg boundary sites, even in the case of trace elements with weak XRF signals.

With regard to the quantitative results, we would like to remark that in the present work we have relied on simple calibrations to relate XRF peak intensities and elemental compositions as obtained by ICP-MS. For instance, to construct the calibrations we have not taken into account the different lithology of the impact layer, the boundary clays and the surrounding marls, which may be expected to yield different matrix effects in the XRF spectra. We would like to stress that, for the sake of rapidness during the field measurements, the samples were measured as collected, without any specific preparation (drying, powdering, etc.). Thus, due to the fact that small flakes of material were directly measured in-situ, it can be expected that the intensity of the XRF peaks may be affected by differences in sample roughness, morphology, etc. As a consequence, and given the experimental uncertainties associated with the lack of sample preparation, we believe that a more involved calibration procedure would not significantly improve the accuracy of the quantitative data obtained by pXRF. These limitations, however, do not reduce the usefulness of the quantitative data thus obtained, which must be considered as semi-quantitative.

Bearing in mind the previous considerations, it is clear that the XRF peak intensities alone (see Figs. 6 and 7), without any further analysis of the data, provide a clear signature of the K-Pg boundary horizon in the case of distal marine settings as those of Agost and Caravaca. Thus, the pXRF technique may become a highly valuable tool to explore and identify K-Pg boundary locations when the field observations fail to do so due to the particular lithologies across the sections or because of an absence of distinctive marker beds in the outcrops (Ellwood et al., 2003; Salih, 2015). The in-situ pXRF measurements might be particularly interesting for the localization of the K-Pg horizon in terrestrial sections, which is highly challenging due to the fact that the sediments are usually highly reworked. A large potential is also envisaged for the detection of the geochemical signature of unreported meteorite impacts, particularly for Precambrian times. More work is thus required to assess the usefulness of pXRF for this type of investigations.

5. Conclusions

In-situ pXRF measurements around the K-Pg impact level at the Agost and Caravaca sections in the SE of Iberian Peninsula have allowed us to detect a sizable enrichment of several elements such as K, Ti, Fe, Ni, Cr, Cu, Zn, As or Pb, together with a strong depletion in the Ca content. These observations represent a primary geochemical signature of the K-Pg boundary in distal marine sections such as those studied in this work. We have also shown that the intensity of selected XRF peaks from these elements correlate well with ICP-MS quantitative data obtained from collected samples. Thus, we conclude that pXRF is a highly valuable tool for the identification and geochemical characterization of possible new K-Pg boundary sites around the world. The technique may also have great potential for the prospection and characterization of other meteorite impacts.

6. Acknowledgements

We gratefully acknowledge the assistance of ICTJA-CSIC XRD laboratory (J. Elvira and S. Alvarez), co-funded by ERDF-EU Ref. CSIC10-4E-141, and of the LabGEOTOP infrastructure, co-funded by ERDF-EU Ref. CSIC08-516 4E-001. This study was carried out within the framework of the Research Consolidated Group GEOPAM (Generalitat de Catalunya, 2014SGR869). VF acknowledges support from the Ministerio de Economía y Competitividad (FPI grant, BES-2012-052366).

References

Alegret L., Molina E. and Thomas E., 2003. Benthic foraminiferal turnover across the Cretaceous/Paleogene boundary at Agost (southeastern Spain): paleoenvironmental inferences. Marine Micropaleontology 48, 251–279.

Alegret L., 2007. Recovery of the deep-sea floor after the Cretaceous–Paleogene boundary event: The benthic foraminiferal record in the Basque–Cantabrian basin and in South-eastern Spain. Palaeogeography, Palaeoclimatology, Palaeoecology 255, 181–194.

Alroy J., 2008. Dynamics of origination and extinction in the marine fossil record. Proc. Natl. Acad. Sci. U.S.A. 105 (suppl. 1), 11536-11542.

Alvarez L. W., Alvarez W., Asaro F. and Michel H. V., 1980. Extraterrestrial cause for the Cretaceous-Tertiary extinction. Science 208 (4448), 1095-1108.

Belza J., Goderis S., Smit J., Vanhaecke F., Baert K., Terryn H. and Claeys P., 2015. High spatial resolution geochemistry and textural characteristics of 'microtektite' glass spherules in proximal Cretaceous–Paleogene sections: Insights into glass alteration patterns and precursor melt lithologies. Geochim. Cosmochim. Acta 152, 1-38.

Bourke A. and Ross P.S., 2015. Portable X-ray fluorescence measurements on exploration drill-cores: comparing performance on unprepared cores and powders for 'whole-rock' analysis. Geochemistry: Exploration, Environment, Analysis 16, 147–157.

Culver S.J., 2003. Benthic foraminifera across the Cretaceous–Tertiary (K–T) boundary: a review. Marine Micropaleontology 47, 177–22.

Ellwood B. B., MacDonald W. D., Wheeler C. and Benoist S. L., 2003. The K-T boundary in Oman: identified using magnetic susceptibility measurements with geochemical confirmation. Earth and Planetary Science Letters 206, 529-540.

Gazley M.F., Vry J.K., Du Plessis E. and Handler M.R., 2011. Application of portable X-ray fluorescence analyses to metabasalt stratigraphy, Plutonic Gold Mine, Western Australia. Journal of Geochemical Exploration 110, 74–80.

Hall G.E.M., Bonham-Carter G.F. and Buchar A., 2014. Evaluation of portable X-ray fluorescence (pXRF) in exploration and mining: Phase 1, control reference materials. Geochemistry: Exploration, Environment, Analysis 14, 99–123.

Keller G., Li L. and MacLeod N., 1996. The Cretaceous/Tertiary boundary stratotype section at El Kef, Tunisia: how catastrophic was the mass extinction?. Palaeogeography, Palaeoclimatology, Palaeoecology 119, 221-254.

Keller G., 2014. Deccan volcanism, the Chicxulub impact, and the end-Cretaceous mass extinction: Coincidence? Cause and effect?. Geological Society of America Special Papers 505, 57-89.

Marsala A.F., Loermans T., Shen S., Scheibe C. and Zereitk R., 2011. Portable energy-dispersive X-ray fluorescence integrates mineralogy and chemostratigraphy into real-time formation evaluation. Petrophysics 53, 102-109.

Martínez-Ruiz F., Ortega-Huertas M., Palomo I. and Barbieri M., 1992. The geochemistry and mineralogy of the Cretaceous–Tertiary boundary at Agost (southeast Spain). Chemical Geology 95, 265–281.

Martínez-Ruiz F., Ortega-Huertas M., Palomo I. and Acquafreda P., 1997. Quench textures in altered spherules from the Cretaceous-Tertiary boundary layer at Agost and Caravaca, SE Spain. Sedimentary Geology 113, 137-147.

Molina E., Alegret L., Arenillas I. and Arz J. A. (2004) El límite Cretácico/Paleógeno del corte de Agost revisado: reconstrucción paleoambiental y patrón de extinción en masa. Journal of Iberian Geology 31, 135-148.

Montanari A., Hay R.L., Alvarez W., Asaro F., Michel H. V., Alvarez L.W. and Smit J., 1983. Spheroids at the Cretaceous-Tertiary boundary are altered impact droplets of basaltic composition. Geology 11, 668-671.

Piercey S.J. and Devine M.C., 2014. Analysis of powdered reference materials and known samples with a benchtop, field portable x-ray fluorescence (pXRF) spectrometer: evaluation of performance and potential applications for exploration lithogeochemistry. Geochemistry: Exploration, Environment, Analysis 14, 139-148.

Potts P. J. and West M. (Eds), 2008. Portable X-Ray Fluorescence Spectrometry: Capabilities for In Situ Analysis. RSC Publishing, Cambridge, England.

Premović P. I., 2011. Distal "Impact" Layers and Global Acidification of Ocean Water at the Cretaceous–Paleogene Boundary (KPB). Geochemistry International 49, 55-65.

Premović P. I., 2015. Cretaceous-Paleogene boundary clays from Spain and New Zeland: Arsenic anomalies. Open Geosciences 1, 721-731.

Raup D. M. and Sepkoski J. J., 1982. Mass Extinctions in the Marine Fossil Record. Science 215, 1501-1503.

Renne P. R., Deino A. L., Hilgen F. J., Kuiper K. F., Mark D. F., Mitchell W. S., Morgan L. E., Mundil M. and Smit, J., 2013. Time scales of critical events around the Cretaceous-Paleogene boundary. Science 339, 684-687.

Rodríguez-Tovar F. J., 2005. Fe-oxide spherules infilling Thalassinoides burrowsat the Cretaceous-Paleogene (KP) boundary: Evidence of a near-contemporaneous macrobenthic colonization during the KP event. Geology 33, 585-588.

Salih M.S., Al-Mutwali M.M. and Aldabbagh S. M., 2015. Geochemical study of the Cretaceous–Tertiary boundary succession exposed at Duhok Dam area (eastern Tethys). Northern Iraq. Arab J. Geosci. 8, 589–603.

Schoene B., Samperton K.M., Eddy M. P., Keller G., Adatte T., Bowring S. A., Khadri S. and Gertsch B., 2014. U-Pb geochronology of the Deccan Traps and relation to the end-Cretaceous mass extinction. Science 347, 182-184.

Schulte P., Deutsch A., Salge T., Berndt J., Kontny A., MacLeod K. G., Neuser R. D. and Krumm S., 2009. Geochim. Cosmochim. Acta 73, 1180-1204

Schulte P. et al., 2010. The Chicxulub asteroid impact and mass extinction at the Cretaceous-Paleogene boundary. Science 327, 1214.

Smit J., 1990. Meteorite impact, extinctions and the Cretaceous-Tertiary Boundary. Geologie en Mijnbouw 69, 187-204.

Smit J., 2004. The section of the Barranco del Gredero (Caravaca, SE Spain): a crucial section for the Cretaceous/Tertiary boundary impact extinction hypothesis. Journal of Iberian Geology 31, 179–191.

Vera J.A., García-Hernández M, López-Garrido A.C., Comas M.C., Puiz-Ortiz P.A. and Martín-Algarra A., 1982. El Cretácico de la Cordillera Bética. In El Cretácico de España (A.García, Ed.), Editorial Complutenca, Madrid, 515-632.

FIGURES

Figure 1. Location of the Cretaceous-Paleogene (K-Pg) boundary at Agost and Caravaca sections in the SE of Iberian Peninsula. The right panels show an overall view of the K-Pg boundary at Agost (top) and Caravaca (bottom) sections.

Figure 2. Stratigraphic column of the Agost section (left) and field photography of the K-Pg horizon and boundary clay (upper picture). The central panels show a SEM image of a microspherule (left) and an EDS spectrum obtained from this spherule (right).

Figure 3. Stratigraphic column of the Caravaca section and field photography of the K-Pg horizon and boundary clay.

Figure 4. Typical XRF spectra of samples from the impact layer and from the Maastrichtian unit from Agost (a) and Caravaca (b) sections.

Figure 5. Example of a lineshape fit (red curve) to extract the intensity of the XRF peaks. The inset shows the linear correlation between the XRF intensities thus obtained with the elemental composition of the samples obtained by ICP-MS.

Figure 6. Normalized intensity (bottom axes) of different XRF peaks for the samples from the Agost section: Ca Kα, Ti Kα, Fe Kα, Cr Kα, Ni Kα, Cu Kα, Zn Kα, Zr Kβ, As Kβ, Pb Lβ, and As Kα + Pb Lα. The upper axes show the corresponding element abundance as obtained from the calibration with laboratory ICP-MS data. The two panels on the right show in detail an area of ±20 cm around the K-Pg boundary (dashed line).

Figure 7. Normalized intensity (bottom axes) of different XRF peaks for the samples from the Caravaca section: Ca Kα, Ti Kα, Fe Kα, Cr Kα, Ni Kα, Cu Kα, Zn Kα, Zr Kβ, As Kβ, Pb Lβ, and As Kα + Pb Lα. The upper axes show the corresponding element abundance as obtained from the calibration with laboratory ICP-MS data. The two panels on the right show in detail an area ±20 cm around the K-Pg boundary (dashed line).

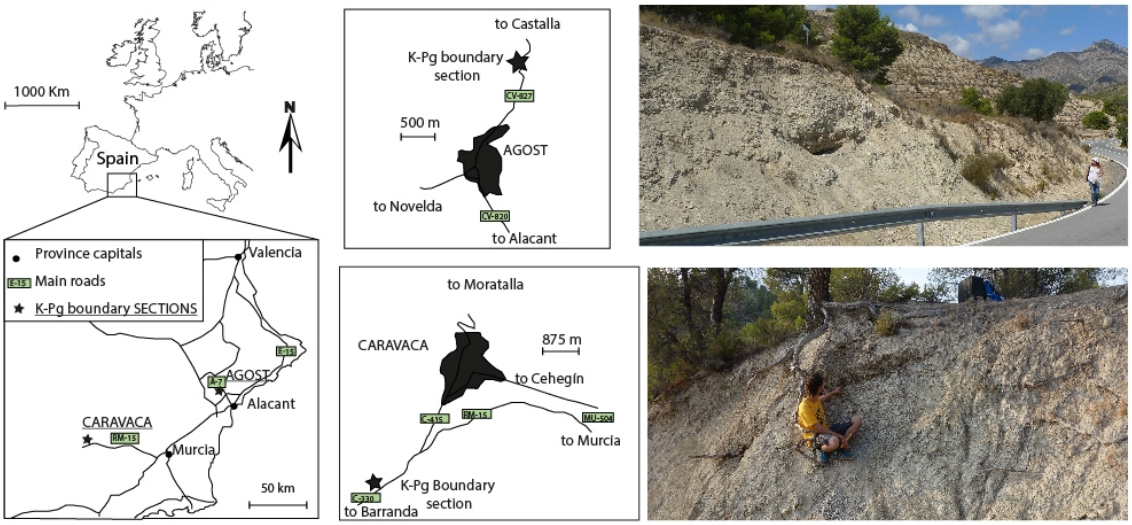
1000 Km
Spain
N
Province capitals
Main roads
K-Pg boundary SECTIONS
Valencia
AGOST
Alacant
CARAVACA
Murcia
50 km
to Castalla
K-Pg boundary section
500 m
AGOST
to Novelda
to Alacant
to Moratalla
CARAVACA
875 m
to Cehegín
to Murcia
K-Pg Boundary section
to Barranda

Figure 1

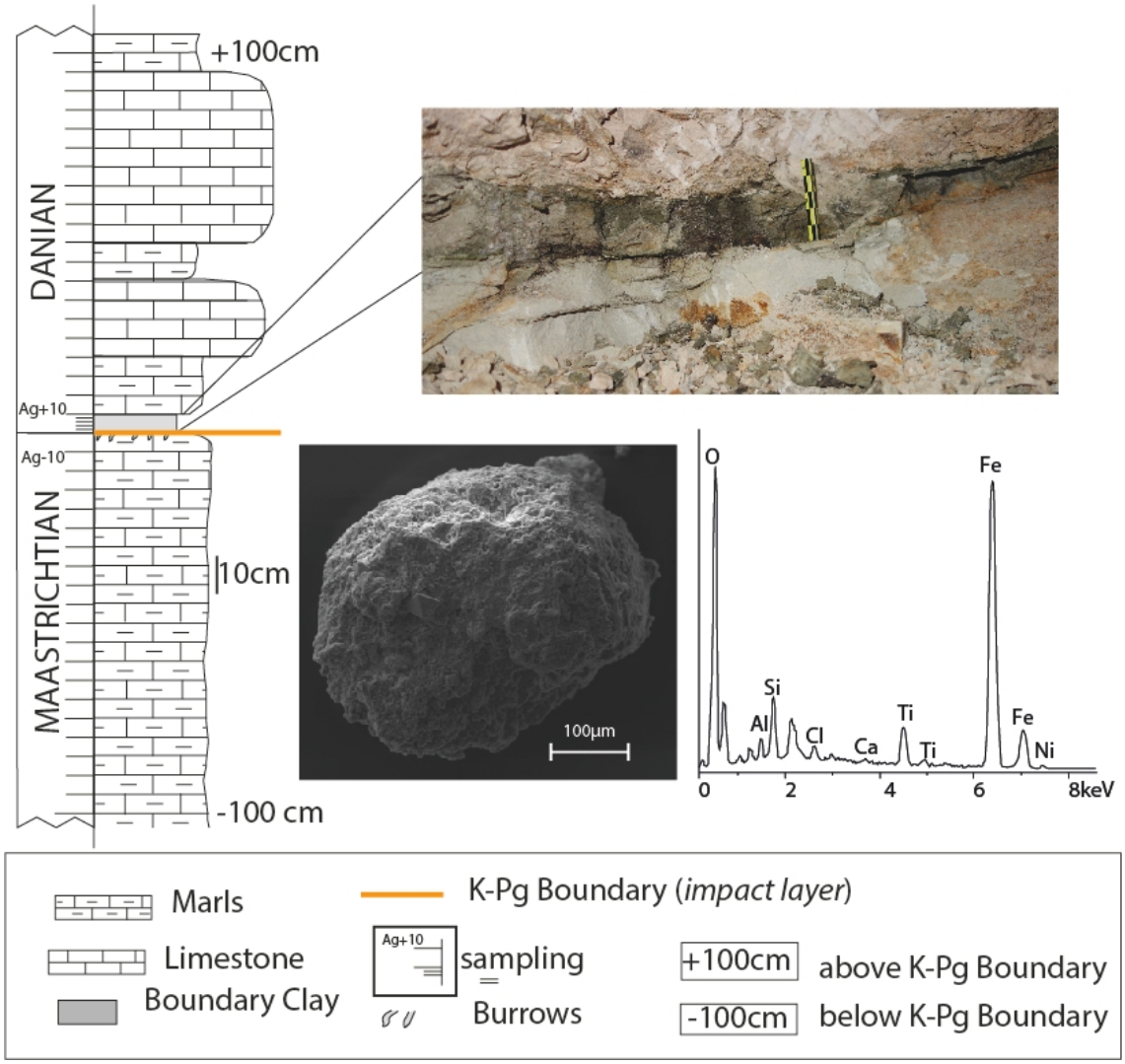
+100cm
DANIAN
Ag+10
Ag-10
MAASTRICHTIAN
10cm
-100 cm
100µm
O
Fe
Si
Al
Cl
Ca
Ti
Ti
Fe
Ni
0
2
4
6
8keV
Marls
Limestone
Boundary Clay
K-Pg Boundary (impact layer)
Ag+10
sampling
Burrows
+100cm
above K-Pg Boundary
-100cm
below K-Pg Boundary

Figure 2

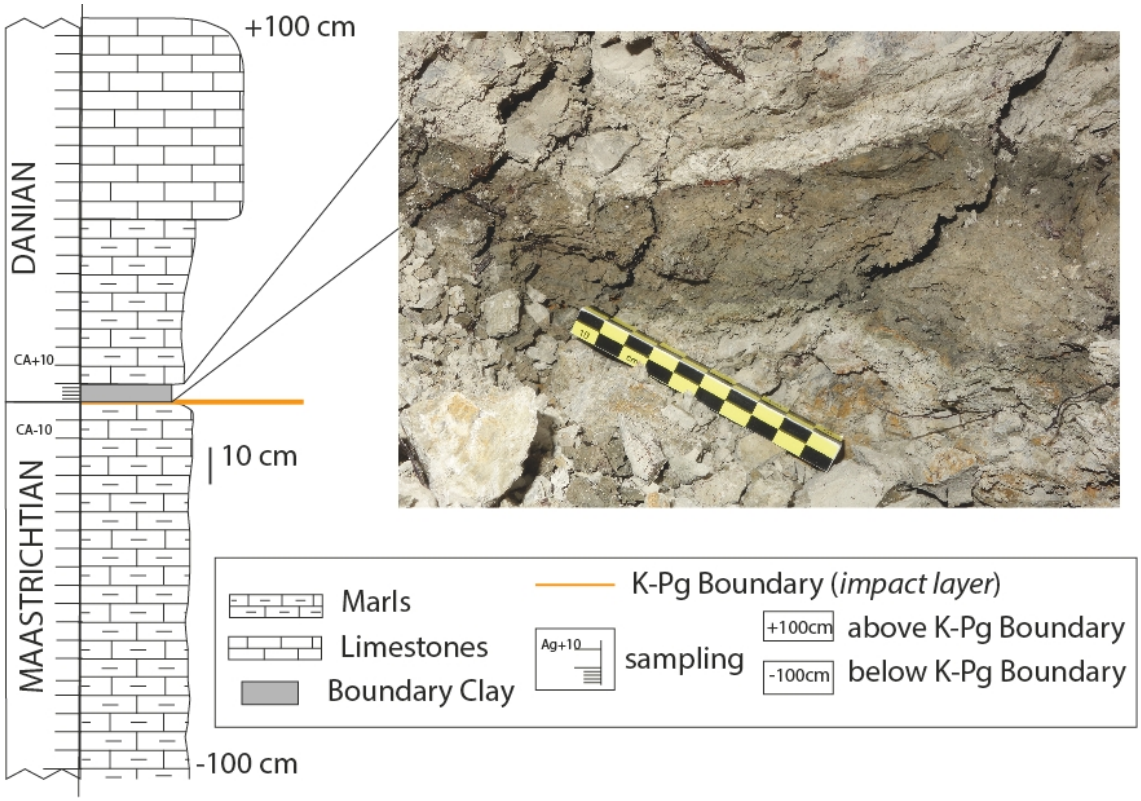
+100 cm
DANIAN
CA+10
CA-10
10 cm
MAASTRICHTIAN
-100 cm
Marls
Limestones
Boundary Clay
K-Pg Boundary (impact layer)
Ag+10
sampling
+100cm
above K-Pg Boundary
-100cm
below K-Pg Boundary

Figure 3

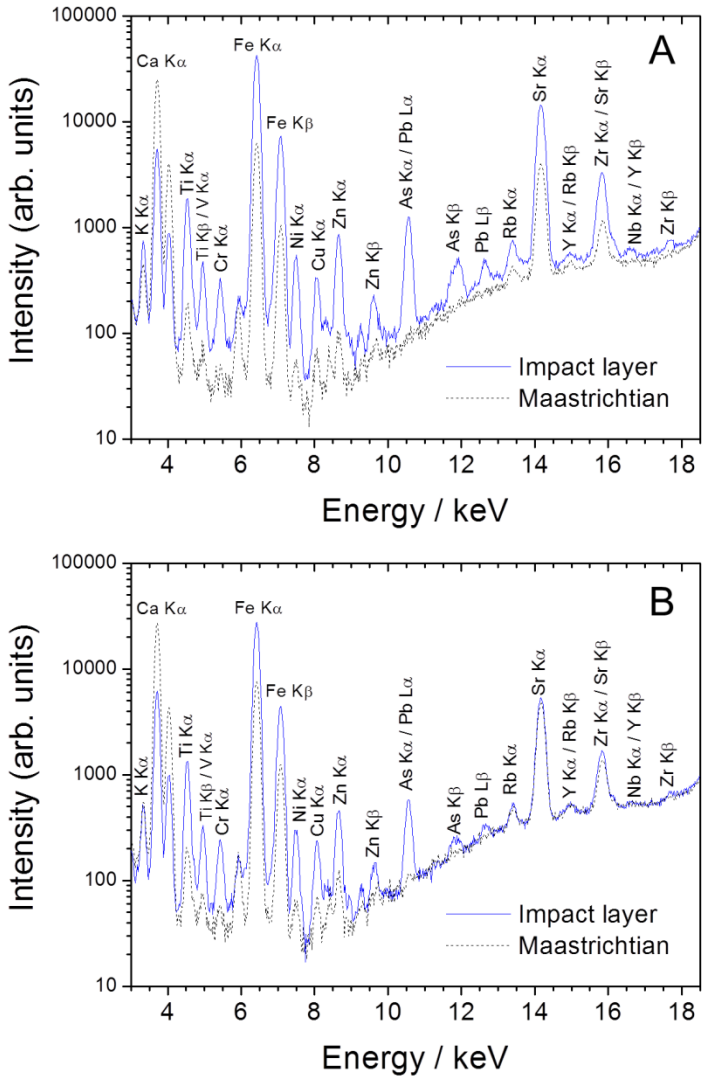
A
B
Intensity (arb. units)
Energy / keV
Impact layer
Maastrichtian
Ca Kα
K Kα
Fe Kα
Fe Kβ
Ti Kα
Ti Kβ / V Kα
Cr Kα
Ni Kα
Cu Kα
Zn Kα
Zn Kβ
As Kα / Pb Lα
As Kβ
Pb Lβ
Rb Kα
Sr Kα
Y Kα / Rb Kβ
Zr Kα / Sr Kβ
Nb Kα / Y Kβ
Zr Kβ

Figure 4

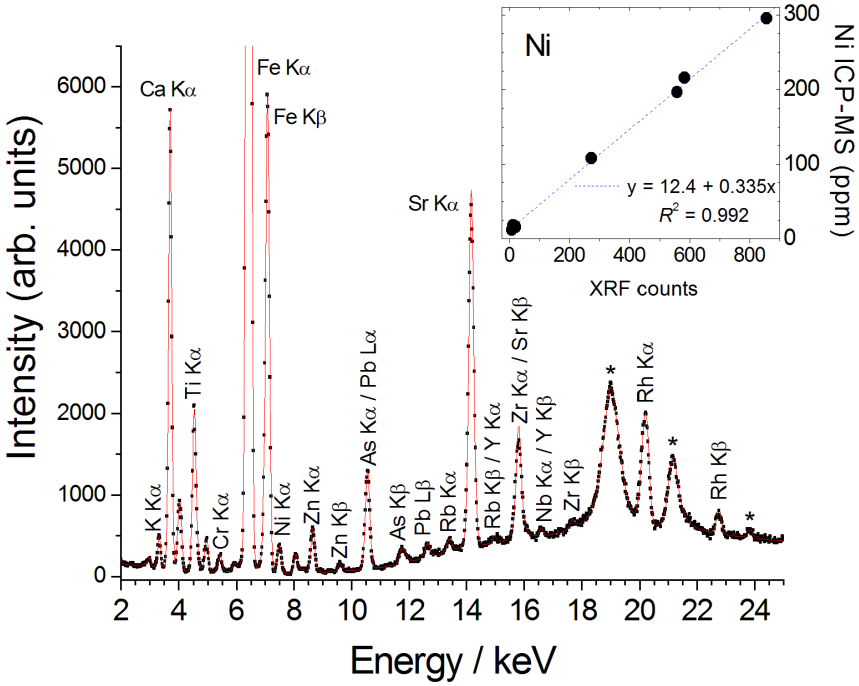
Intensity (arb. units)
Energy / keV
Ca Kα
Fe Kα
Fe Kβ
Sr Kα
Ti Kα
K Kα
Cr Kα
Ni Kα
Zn Kα
Zn Kβ
As Kα / Pb Lα
As Kβ
Pb Lβ
Rb Kα
Rb Kβ / Y Kα
Zr Kα / Sr Kβ
Nb Kα / Y Kβ
Zr Kβ
Rh Kα
Rh Kβ
*
Ni
y = 12.4 + 0.335x
R2 = 0.992
XRF counts
Ni ICP-MS (ppm)

Figure 5

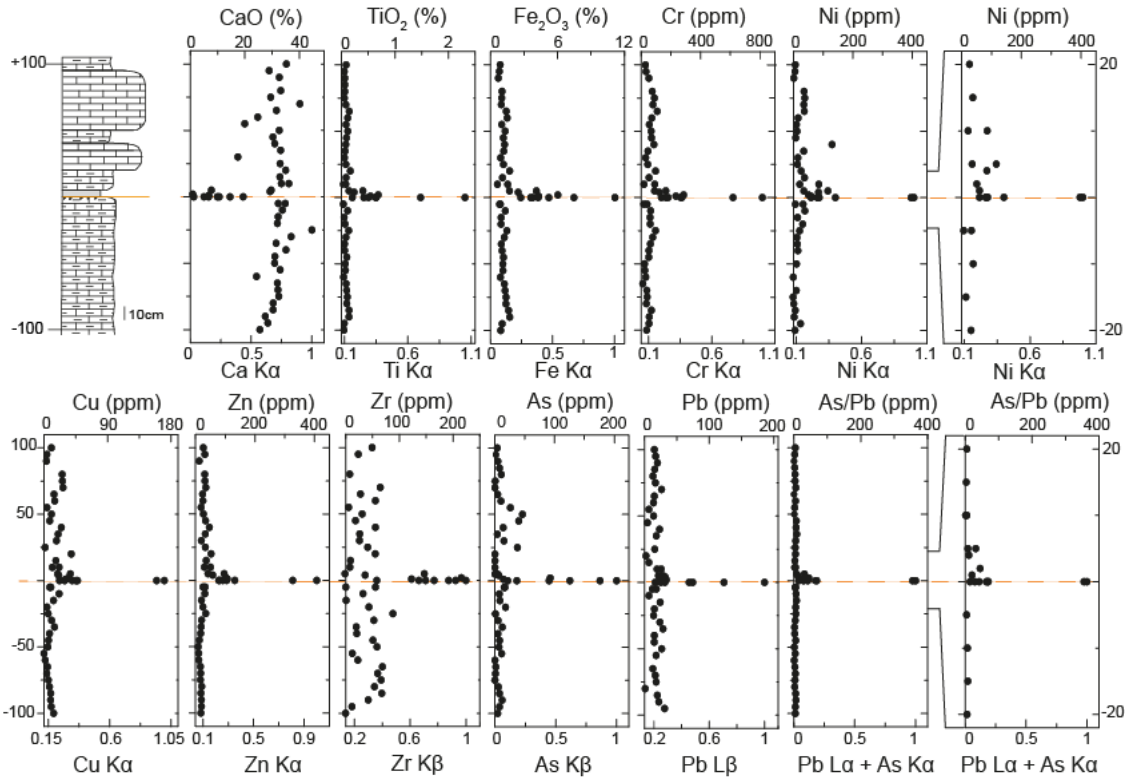
CaO (%)
TiO2 (%)
Fe2O3 (%)
Cr (ppm)
Ni (ppm)
Ni (ppm)
+100
-100
10cm
Ca Kα
Ti Kα
Fe Kα
Cr Kα
Ni Kα
Ni Kα
Cu (ppm)
Zn (ppm)
Zr (ppm)
As (ppm)
Pb (ppm)
As/Pb (ppm)
As/Pb (ppm)
Cu Kα
Zn Kα
Zr Kβ
As Kβ
Pb Lβ
Pb Lα + As Kα
Pb Lα + As Kα

Figure 6

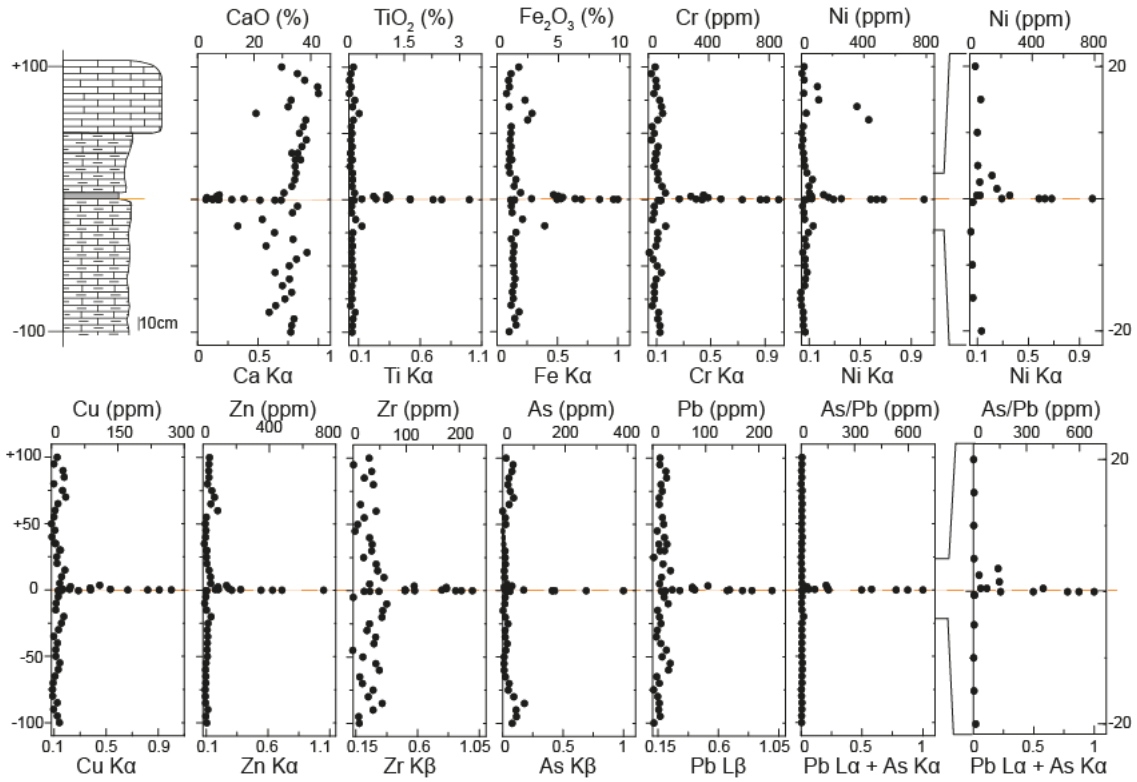
CaO (%)
TiO2 (%)
Fe2O3 (%)
Cr (ppm)
Ni (ppm)
Ni (ppm)
+100
-100
10cm
Ca Kα
Ti Kα
Fe Kα
Cr Kα
Ni Kα
Ni Kα
Cu (ppm)
Zn (ppm)
Zr (ppm)
As (ppm)
Pb (ppm)
As/Pb (ppm)
As/Pb (ppm)
+50
0
-50
Cu Kα
Zn Kα
Zr Kβ
As Kβ
Pb Lβ
Pb Lα + As Kα
Pb Lα + As Kα

Figure 7

Highlights

- Testing of Xray fluorescence to identify geochemical anomalies in the geological record.
- Correlation of elementary XRF intensities with ICP-MS data
- Identification of increasing Ti, Fe, Cr, Ni, Cu or Pb anomalies and decrease of Ca at boundary